Doping-induced change of optical properties in underdoped cuprate superconductors

1999 J. Phys.: Condens. Matter 11 239

(http://iopscience.iop.org/0953-8984/11/1/020)

J. Phys.: Condens. Matter **11** (1999) 239–264. Printed in the UK PII: S0953-8984(99)96100-3

Doping-induced change of optical properties in underdoped cuprate superconductors

H L Liu†*, M A Quijada†#, A M Zibold†, Y-D Yoon†, D B Tanner†, G Cao‡, J E Crow‡, H Berger§, G Margaritondo§, L Forró‖, Beom-Hoan O¶, J T Markert¶, R J Kelly+ and M Onellion+

† Department of Physics, University of Florida, Gainesville, FL 32611, USA
‡ National High Magnetic Field Laboratory, Florida State University, Tallahassee, FL 32306, USA
§ Institute de Physique Appliquée, Ecole Polytechnique Fédérale de Lausanne, PHB Ecublens, 1015 Lausanne, Switzerland
‖ Institute de Génie Atomique, Ecole Polytechnique Fédérale de Lausanne, PHB Ecublens, 1015 Lausanne, Switzerland
¶ Department of Physics, University of Texas, Austin, TX 78712, USA
+ Department of Physics, University of Wisconsin, Madison, WI 53706, USA

Received 21 July 1998

Abstract. We report on the *ab*-plane optical reflectance measurements of single crystals of Y-doped $Bi_2Sr_2CaCu_2O_{8+\delta}$ and Pr-doped $YBa_2Cu_3O_{7-\delta}$ over a wide frequency range from 80 to 40 000 cm^{-1} (10 meV–5 eV) and at temperatures between 20 and 300 K. Y and Pr doping both decrease the hole concentration in the CuO_2 planes. This has allowed us to investigate the evolution of *ab*-plane charge dynamics at doping levels ranging from heavily underdoped to nearly optimally doped. Our results of the low-frequency optical conductivity and spectral weight do not show any features associated with the normal-state pseudogap. Instead, one-component analysis for the optical conductivity shows the low-frequency depression in the scattering rate at $T > T_c$, signalling entry into the pseudogap state. Alternatively, no clear indications of the normal-state pseudogap are detected in the temperature-dependent zero-frequency free-carrier scattering rate by using two-component analysis. In the superconducting state, there is also no convincing evidence of superconducting gap absorption in all spectra. We find that there is a 'universal correlation' between the numbers of carriers and the transition temperature. This correlation holds whether one considers the number of carriers in the superfluid or the total number of carriers.

1. Introduction

The subject of normal-state properties in the underdoped high-T_c superconductors has received a great deal of attention recently [1]. This interest is exemplified by the so-called 'normal-state pseudogap' phenomenon observed in several different experimental techniques. The nuclear magnetic resonance (NMR) [2–5] and neutron-scattering measurements [6, 7] first suggested the opening of a gap in the spin excitation spectrum on normal-state underdoped $YBa_2Cu_3O_{7-\delta}$ (Y123) and $YBa_2Cu_4O_8$ (Y124). More recently, gap-like features in the charge excitation spectrum of underdoped Y123 and $Bi_2Sr_2CaCu_2O_{8+\delta}$ (Bi2212) have been inferred from or directly observed in measurements of the specific heat [8], the dc resistivity [9–11],

* Present address: Department of Physics, University of Illinois at Urbana-Champaign, Urbana, IL 61801, USA.
# Present address: Code 551, Goddard Space Flight Center, Greenbelt, MD 20771, USA.

Raman spectroscopy [12–14], tunnelling spectroscopy [15] and angle-resolved photoemission spectroscopy (ARPES) experiments [16–19] at characteristic temperatures T^* well above T_c.

Indications of normal-state, gap-like anomalies in underdoped cuprates were observed in infrared optical measurements as well [20–25]. The c-axis spectra of underdoped Y123 [20, 21] and Y124 [22] show a suppression of optical conductivity below 400 cm^{-1} at $T > T_c$, which is interpreted as the result of the formation of a pseudogap. This spectral feature appears at a temperature scale which matches the spin susceptibility determined from the NMR measurements and has been discussed in the context of the spin gap. In contrast, a pseudogap is not evident in the ab-plane optical conductivity. Instead, there is a depressed scattering rate $1/\tau(\omega, T)$ at low frequencies and at temperatures a little above T_c [23–25]. The shape of the normal-state and the superconducting-state $1/\tau(\omega, T)$ are very close.

There are several open questions about this normal-state pseudogap observed in the optical spectroscopy. First, the energy of the pseudogap-like structure does not change with doping. It is commonly observed at 400 cm^{-1} in the c-axis conductivity and around 700 cm^{-1} in the ab-plane scattering rate. Also, it is unclear why there is an apparent factor of two between these two energy scales. Second, the doping independence of the energy is in strong contrast to the behaviour of spin gap temperature, which decreases with doping. Third, the normal-state in-plane conductivity exhibits a much larger spectral weight at high frequencies than would be present from the generalized Drude form with a frequency-dependent lifetime.

In order to address the above issues we have measured the ab-plane reflectance of single crystals of Y-doped Bi2212 and Pr-doped Y123 with changes in carrier densities at doping levels ranging from heavily underdoped to nearly optimally doped. Optical investigations, extending over a broad frequency range and at various temperatures, offer an effective way to study the energy and temperature dependence of intrinsic parameters characterizing these materials. We first describe a number of optical properties: the reflectance spectrum, the optical conductivity, and the effective carrier density. We then discuss how they might account for the evolution of the ab-plane spectrum with doping. Next, we focus on the low-frequency conductivity and spectral weight of a strongly underdoped Bi2212 sample ($T_c = 35$ K) in the whole temperature range. We investigate whether the normal-state pseudogap leads to a change of the charge excitation spectrum that can account for the observed dc resistivity. Of particular relevance in this connection, is the identification of the energy and temperature dependence of the quasiparticle damping. We derive the scattering rate from both the one-component and the two-component pictures. In one-component analysis, our results have been treated within the framework of the generalized Drude model and the marginal Fermi liquid theory [26, 27]. Depending on the model, we compare the different features in the scattering rate deduced from the spectra. To the end, considering the superconducting response for all doping levels studied, observation of a superconducting gap has been a hotly disputed issue. Even though we cannot say anything definite about the superconducting gap in all our spectra, the amount of conductivity that condenses into the δ function at $\omega = 0$ is given less ambiguously from infrared measurements. Our discussion will focus on the relation between the transition temperature and the number of carriers in the superfluid or the total number of carriers.

2. Experiment

2.1. Sample characteristics

The optical experiments were performed on Bi2212 and Y123 single crystals. In these systems, there are two ways to reduce the carrier concentration in the CuO_2 planes, and, thus prepare

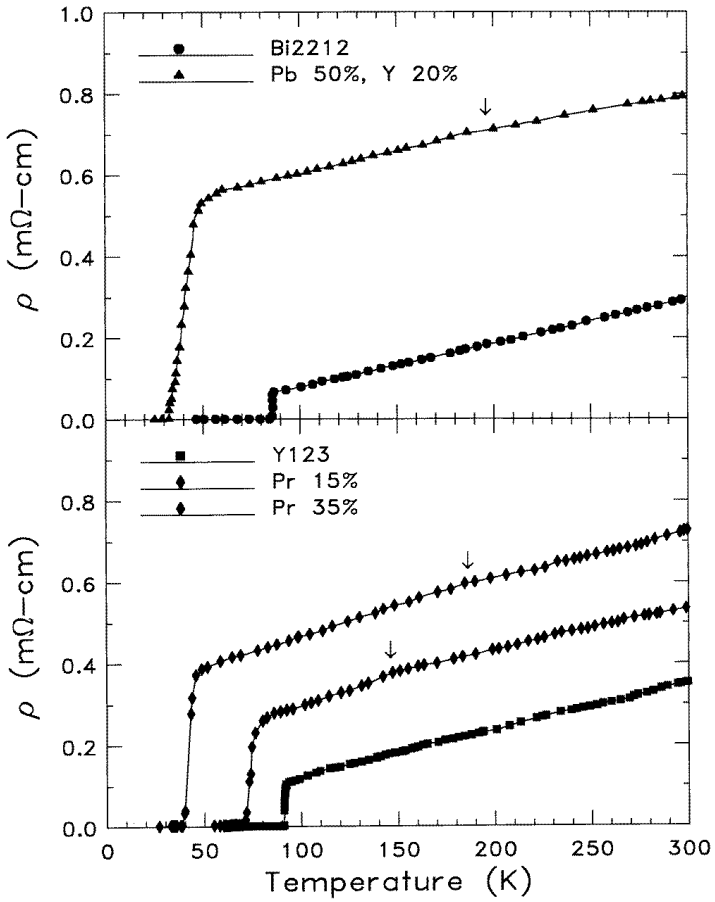

Figure 1. Temperature dependence of the *ab*-plane resistivity for Y-doped $Bi_2Sr_2CaCu_2O_{8+\delta}$ and Pr-doped $YBa_2Cu_3O_{7-\delta}$ single crystals, measured by a four-probe method. A characteristic change of slope $d\rho/dT$ at temperature T^* is marked by arrows.

underdoped samples. One is to substitute an element in the crystal structure by another one with higher valence state. In this case the substitution of Y^{3+} for Ca^{2+} has been found to be most efficient in Bi2212 [28]. Heavily underdoped Bi2212 samples with $T_c = 35$ K (Pb 50%, Y 20%), 40 K (Y 35%) were measured. Another way is to remove oxygen from the pure samples. By annealing the crystals under a flowing argon gas, one slightly underdoped Bi2212 with $T_c = 85$ K was obtained. Details of sample preparation have been reported elsewhere [29]. In the Y123 system, we studied three fully oxygenated $Y_{1-x}Pr_xBa_2Cu_3O_{7-\delta}$ single crystals. Substitution of Pr for the Y atom in Y123 changes only the hole content in the CuO_2 planes, while the structure of the CuO chains remains unaffected [30]. The Pr-doped samples have a T_c of 92, 75 and 40 K, respectively, for $x = 0$, 0.15 and 0.35. The crystals were grown by a method described elsewhere [31].

The dc resistivity measurements as a function of temperature on five samples are depicted in figure 1. The resistivities of Bi2212 and Y123, with a $T_c = 85$, 92 K, follow a linear curve over a wide temperature range. At 300 K, the increase of the resistivity with Y or Pr doping is apparently due to the reduction of the carrier concentration, although disorder introduced

by the doping may also contribute to this increase. Interestingly, as in all doped samples, the overall resistivity still shows metallic-like behaviour down to the transition temperature. However, there is a characteristic change of slope $d\rho/dT$ at temperature T^* marked by arrows. The values of T^* increase with increasing Y and Pr doping. This feature is similar to the one observed in underdoped Y123 by oxygen removal [11] and Sr-doped $La_{2-x}Sr_xCuO_4$ (La214) [32, 33]. Since it is less likely that the number of carriers increases below T^*, it appears that the temperature dependence of the normal-state resistivity $\rho = (m/ne^2)(1/\tau)$ must be attributed entirely to the scattering rate. Thus, a slope change in the resistivity below T^* indicates a change of carrier scattering at low temperatures.

2.2. Optical measurements

The optical reflectance of all crystals were measured for the radiation polarized parallel to the *ab*-plane over 80–40 000 cm^{-1} (10 meV–5 eV). In the high frequency (1000–40 000 cm^{-1}) range we use a Perkin–Elmer 16U grating spectrometer while the far- and mid-infrared (80–4000 cm^{-1}) regions were measured with a Bruker IFS 113v Fourier transform spectrometer. For the later frequencies, the temperature of the sample was varied between 300 and 20 K by using a continuous-flow cryostat with a calibrated Si-diode thermometer mounted nearby. Determination of the absolute value of the reflectance was done by coating the sample with a 2000 Å film of aluminum after measuring the uncoated sample. The spectra of the uncoated sample were then divided by the obtained spectrum of the coated sample and corrected for the know reflectance of aluminum. The accuracy in the absolute reflectance is estimated to be ±1%.

The optical properties (i.e. the complex conductivity $\sigma(\omega) = \sigma_1(\omega) + i\sigma_2(\omega)$) were calculated from Kramers–Kronig analysis of the reflectance data. The usual requirement of the Kramers–Kronig integrals to extend the reflectance at the low- and high-frequency ends was done in the following way. At low frequencies, the extension was done by modelling the reflectance using a Drude–Lorentz model and using the fitted results to extend the reflectance below the lowest frequency measured in the experiment. The high-frequency extrapolations were done by merging the data with results from the literature [34] or by using a weak power law dependence, $\mathcal{R} \sim \omega^{-s}$ with $s \sim 1$–2. The highest frequency range was extended with a power law $\mathcal{R} \sim \omega^{-4}$, which is the free-electron behaviour limit.

3. Results

3.1. Room-temperature spectra

Figure 2 shows the room-temperature *ab*-plane reflectance of the six crystals over the entire spectral range. Note the logarithmic scale. The reflectance of each sample drops steadily (but not quite linearly) throughout the infrared, with a sort of plasmon minimum around 8000–15 000 cm^{-1} in all cases. What is notable about the two highest-T_c crystals of Bi2212 and Y123 is that they show high values of reflectance over 90% for $\omega < 1000\ cm^{-1}$. For the doped samples, with reduced carrier concentration in the CuO_2 planes, the reflectance in the whole infrared region is substantially decreased. As a consequence, a few infrared-active phonons in the *ab*-plane are visible. However, this reduction of the carrier density has little effect on the frequency location of the plasmon minimum. It is interesting to note that there is a shoulder at ∼4000 cm^{-1} in Y123 systems, which is probably associated with excitations on the *b*-axis-oriented chains. Such a feature was also observed in the optical measurements of single-domain Y123 crystals [35].

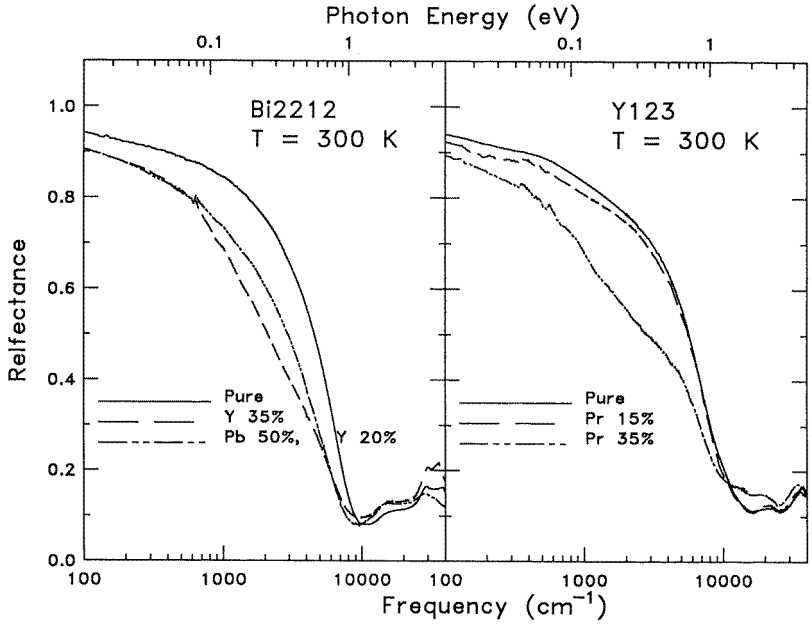

Figure 2. The room-temperature *ab*-plane reflectance of six crystals over the entire frequency range.

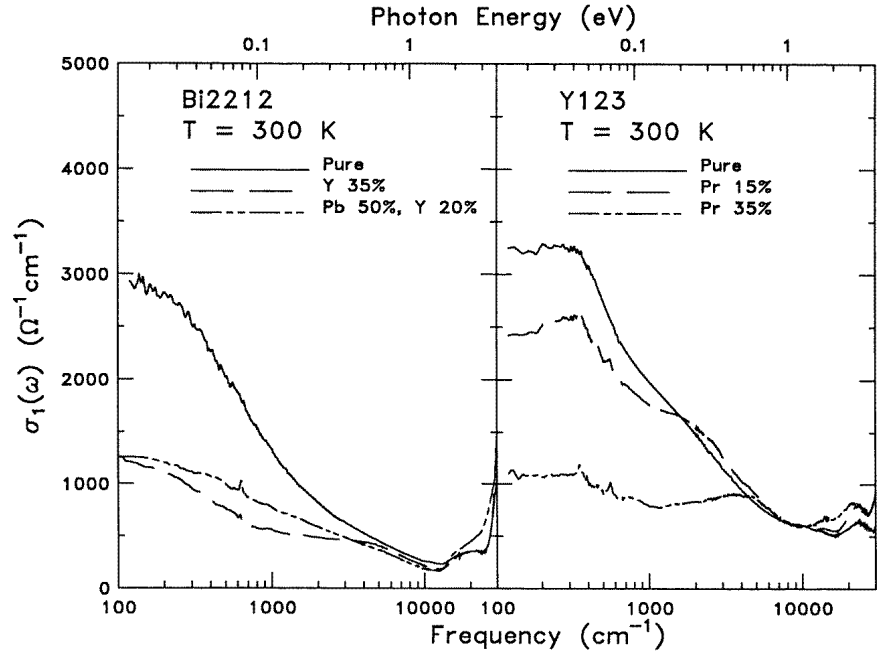

Figure 3. The real part of the optical conductivity $\sigma_1(\omega)$ obtained by Kramers–Kronig analysis of the room-temperature reflectance presented in figure 2.

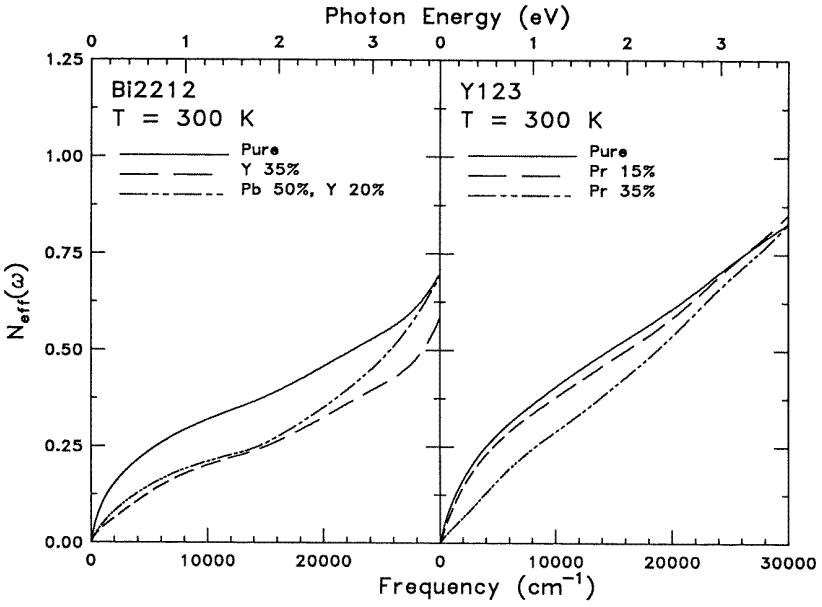

Figure 4. The effective number of carriers per planar Cu atom $N_{\rm eff}(\omega)$ obtained by the integration of $\sigma_1(\omega)$ up to a certain frequency, as described in equation (1).

The real part of the optical conductivity $\sigma_1(\omega)$, obtained from Kramers–Kronig analysis of the reflectance, is shown in figure 3. The *ab*-plane optical conductivity spectra of the Bi2212 and Y123 near optimal doping have several common features. There is a peak at $\omega = 0$ and a long tail extending to higher frequencies in the infrared region where $\sigma_1(\omega)$ falls as ω^{-1}, slower than ω^{-2} decay of a Drude spectrum. At higher frequencies, we observe the onset of the charge-transfer absorption at $\sim$14 000 cm^{-1}, which corresponds to the optical transition between the occupied O 2p band and the empty Cu 3d upper Hubbard band. Other interband transitions appear above 20 000 cm^{-1}. In the reduced-T_c samples, as suggested by the reflectance data in figure 2, there is a lot of spectral weight lost in the infrared region. Significantly, the weight lost below the charge-transfer absorption band is transferred to the higher frequencies. Note that the Y123 crystals show a bump-like structure around 4000 cm^{-1} on account of the excitations in the chains mentioned above. Finally, weak phonon modes, which are not completely screened by the free carriers, are seen in the far infrared.

Additional information about the electronic structure can be extracted from the oscillator strength sum rule [36]. The effective number of carriers participating in optical transitions for energies less than $\hbar\omega$ is given by

$$\left[\frac{m}{m^*}\right] N_{\rm eff}(\omega) = \frac{2mV_{\rm cell}}{\pi e^2 N_{\rm Cu}} \int_0^{\omega} \sigma_1(\omega')\,{\rm d}\omega' \qquad (1)$$

where m^* is the effective mass of the carriers, m is the free-electron mass, $V_{\rm cell}$ is the unit cell volume and $N_{\rm Cu}$ is the number of CuO layers per unit cell. Here, we use $N_{\rm Cu} = 2$ for all measured twinned single crystals. The effective mass is taken as the free-electron value. A plot of $N_{\rm eff}(\omega)$ per planar Cu atom is shown in figure 4 on a linear scale. For the crystals with high dc conductivity, $N_{\rm eff}(\omega)$ at first increases steeply at low frequencies, on account of the appearance of a Drude-like band centred at $\omega = 0$, and continues to increase in the mid-infrared region. $N_{\rm eff}(\omega)$ exhibits a plateau in the interval between 6000 and 12 000 cm^{-1}.

Above 12 000 cm^{-1}, the remaining charge-transfer excitation and higher-frequency transitions contribute $N_{\rm eff}(\omega)$. As expected, decreasing $N_{\rm eff}(\omega)$ over a wide frequency range was observed in the low T_c samples. However, all $N_{\rm eff}(\omega)$ curves come together above 30 000 cm^{-1}. This shows that, for reducing carrier numbers, the low-frequency spectral weight shifts to high frequency but the total weight does not change below 30 000 cm^{-1}. Indeed, the redistribution of the spectral weight in the CuO_2 planes with doping was previously observed for Sr-doped La214 [37] and oxygen-deficient Y123 [38, 39].

3.2. Temperature dependence in the infrared

The temperature dependence of the *ab*-plane infrared conductivity is shown in figure 5. The optical response of all samples is metallic, i.e. when the temperature is lowered from 300 K, there is an increase in $\sigma_1(\omega)$ at the lowest frequencies, in accord with the decreasing dc resistivity. As mentioned above, for $T > T_c$, $\sigma_1(\omega)$ is strongly suppressed in underdoped samples over the entire infrared frequency range. Nevertheless, the conductivity below 300–400 cm^{-1} remains approximately Drude-like: a zero-frequency peak which grows and sharpens

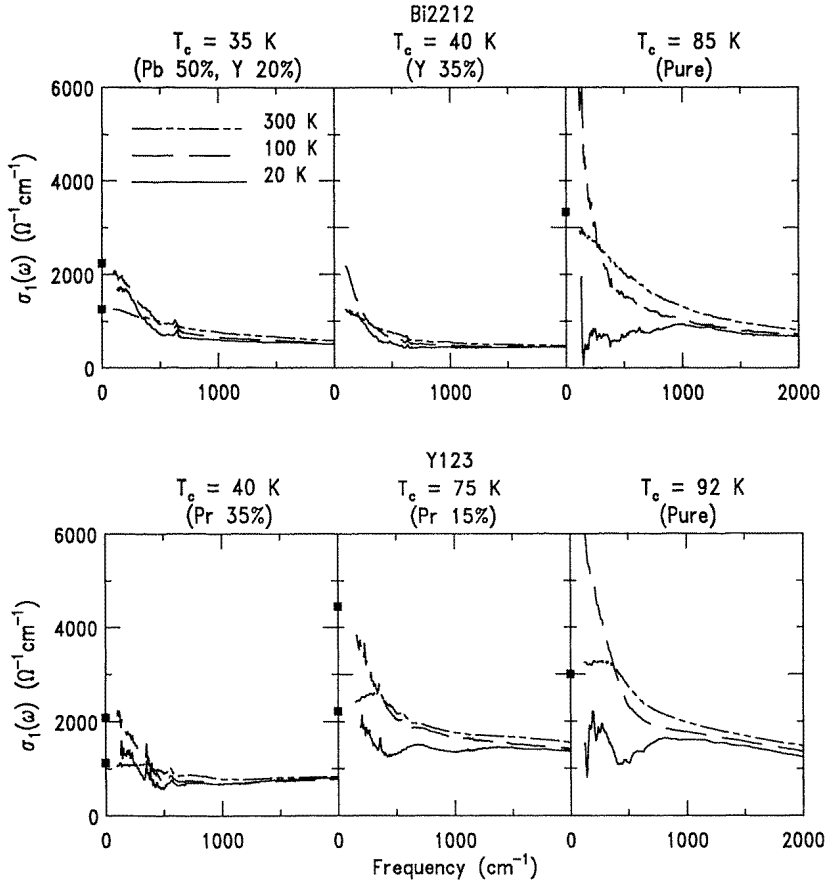

Figure 5. The far- and mid-infrared optical conductivity of six samples at 20, 100 and 300 K. The symbols show the dc conductivity values.

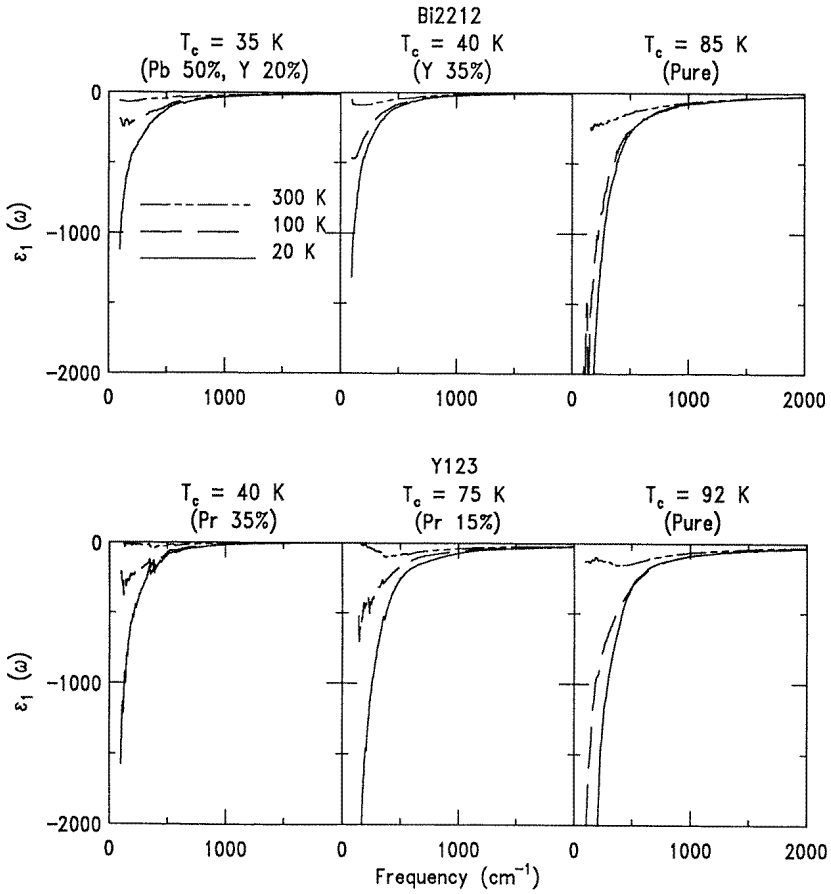

Figure 6. The real part of the dielectric function $\epsilon_1(\omega)$ obtained by Kramers–Kronig analysis of the reflectance data. The data shown are from $\omega \sim 100$ to 2000 cm^{-1} at 20, 100 and 300 K.

as temperature is reduced. The temperature dependence at frequencies above 1000 cm^{-1} is relatively modest; it is in fact mostly due to a narrowing of the Drude-like peak at zero frequency. Below T_c, there is a transfer of oscillator strength from the far-infrared region to the zero-frequency δ-function response of the superconducting condensate [40]. The spectral weight lost at low frequencies in the superconducting state is large in the nearly optimally doped samples while in most underdoped samples it is very small. It should be noted that for all doping levels studied, at 20 K, there remains a pronounced conductivity at low frequencies, suggesting no sign of a superconducting gap.

Figure 6 shows the real part of the dielectric function at three temperatures below 2000 cm^{-1}. The rapid decrease in $\epsilon_1(\omega)$ of all the samples at low frequency with decreasing temperature is an indication of the metallic behaviour (characteristic of free carriers). In a purely Drude system, the zero crossing corresponds to the location of the screened plasma frequency, $\tilde{\omega}_p = \omega_p/\sqrt{\epsilon_\infty}$ where ϵ_∞ is the background dielectric associated with the high-frequency interband transitions, and the plasma frequency ω_p is related to the carrier density n through $\omega_p = \sqrt{4\pi ne^2/m^*}$. However, the cuprates are not simple metals, and the presence of a number of excitations in the mid-infrared will tend to shift the zero crossing to a lower

frequency. Thus, estimate of carrier density should be made from $N_{\rm eff}(\omega)$ instead of $\tilde{\omega}_p$. As the temperature is lowered below T_c, $\epsilon_1(\omega)$ shows a large negative value, implying that the inductive current dominates over the conduction current in the superconducting state. Here, the dielectric function looks like that of perfect free carriers; $\epsilon_1(\omega) = \epsilon_\infty - \omega_{pS}^2/\omega^2$ where $\omega_{pS} = \sqrt{4\pi n_s e^2/m^*}$ is the superfluid plasma frequency and n_s is the superfluid density. The reduced n_s is quite evident in the doped samples in the figure 6.

4. Discussion

4.1. Low-frequency spectral functions

As noted previously, ARPES experiments [16–18] on underdoped Bi2212 crystals in the normal state revealed the existence of a pseudogap in the charge excitation spectrum—a suppression of spectral weight with a residual intensity on the Fermi level. For a next step, in order to investigate the influence that the pseudogap has on the peculiar charge dynamics of the CuO_2 planes, we present a complete set of temperature-dependent data in the most underdoped Bi2212 with $T_c = 35$ K. Our other underdoped Bi2212 and Y123 samples gave similar results. We emphasize two important spectral functions, the real part of the conductivity $\sigma_1(\omega, T)$ and a dimensionless measure of spectral weight $N_{\rm eff}(\omega, T)$.

4.1.1. Optical conductivity. The temperature evolution in $\sigma_1(\omega, T)$ is shown in figure 7. In the normal state, $\sigma_1(\omega, T)$ approaches the ordinary dc conductivity at low frequencies. The dc conductivity is shown on the vertical axis as filled squares. At the same time, we observe a narrowing in the far-infrared conductivity at low temperatures, whereas at higher frequency, $\sigma_1(\omega)$ does not show much temperature variation. If there is indeed the formation of an energy gap at the Fermi surface in normal-state superconducting cuprates at low hole densities, from ARPES, at least in underdoped Bi2212, the corresponding optical conductivity spectrum should exhibit a bump-like structure. The situation must be similar to an interband transition like the charge-transfer band in the cuprates. Note also that the opening of a pseudogap in the electronic spectrum is clearly seen in the c-axis conductivity of Y123 and Y124 [20–22]. In contrast to this, no distinct features are observed in the infrared ab-plane $\sigma_1(\omega, T)$ for our underdoped Bi2212 crystals. Although we cannot rule out the possibility that disorder introduced by the doping may influence the observability of the normal-state pseudogap, other experimental techniques including Raman [12, 14] and ARPES [16–19] measurements on the similar underdoped Bi2212 indeed reveal the presence of a gap in the charge excitation spectrum at certain locations on the Fermi surface. Additionally, in underdoped cuprates which exhibit a pseudogap, there is convincing evidence that the lattice responds to this change in the electronic spectrum [41, 42]. In figure 7, there is a strong phonon resonance at $\sim$630 cm^{-1} in the whole temperature range. We believe this phonon is the ordinary in-plane vibration. The phonon frequency hardens by 14 cm^{-1} as the sample cools from 300 to 20 K and no anomalies at either T^* or T_c are observed.

4.1.2. Spectral weight shift. We now turn to an analysis of the $N_{\rm eff}(\omega, T)$ function, which is plotted in figure 8 and obtained by numerical integration (equation (1)) of $\sigma_1(\omega, T)$ in figure 7. In the normal state, the spectral weight associated with the free carriers shifts to lower frequency with decreasing temperature, on account of the sharpening of the Drude-like peak in $\sigma_1(\omega)$. This is reflected in the rapid increase in the value of $N_{\rm eff}(\omega, T)$ at low frequency. A more detailed look of the temperature dependence of the low-frequency spectral

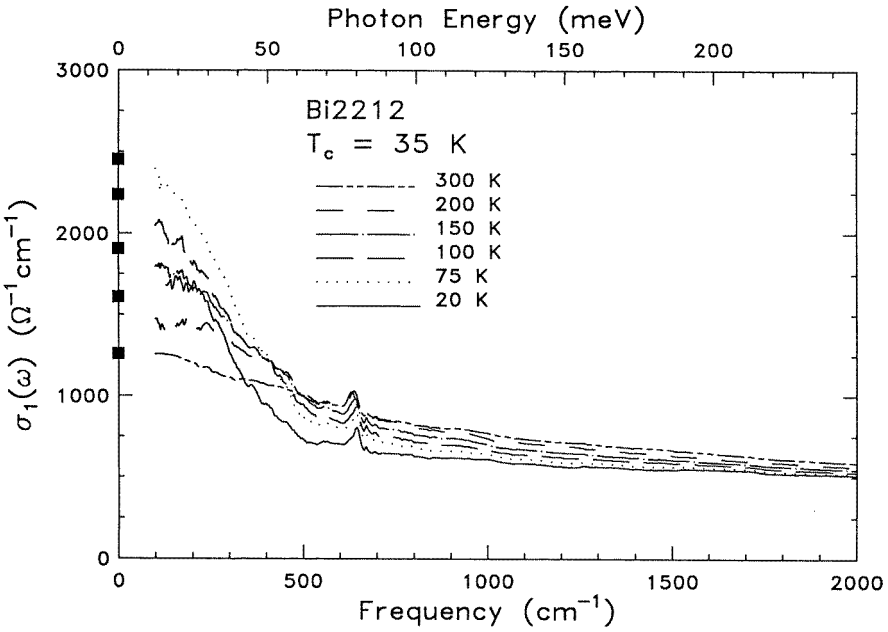

Figure 7. The infrared optical conductivity for Y-doped $Bi_2Sr_2CaCu_2O_{8+\delta}$ (T_c = 35 K) at temperatures between 20 and 300 K. The dc conductivity values are indicated by the symbols.

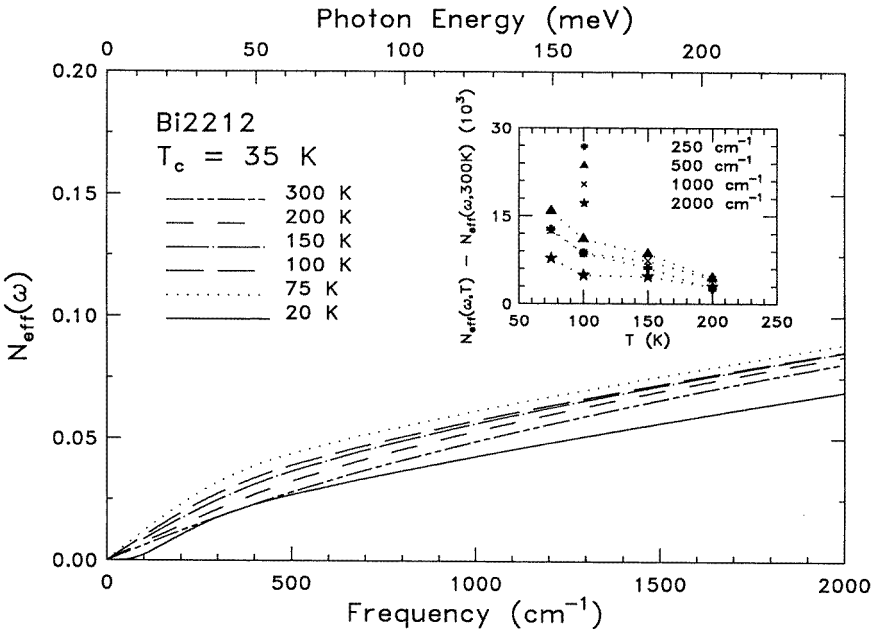

Figure 8. The partial sum-rule spectrum per planar Cu atom, $N_{\rm eff}(\omega, T)$, for Y-doped $Bi_2Sr_2CaCu_2O_{8+\delta}$ (T_c = 35 K) at temperatures between 20 and 300 K. The inset shows the difference in $N_{\rm eff}(\omega, T)$ computed at 300 K and other lower temperatures for ω = 250, 500, 1000 and 2000 cm^{-1}.

weight is given in the inset of figure 8. We plot the difference in $N_{\rm eff}(\omega, T)$ computed in the 300 K and other lower temperatures for $\omega = 250$, 500, 1000 and 2000 cm^{-1}. Again, the gradual increase of the spectral weight is observed at each frequency from 200 to 75 K. If there were a pseudogap to develop in the charge carrier excitation spectrum for underdoped Bi2212, as suggested by ARPES measurements [16–18], one would expect an influence on the low-frequency spectral weight from the gapping of some of the carriers at particular parts of the Fermi surface. This modification of the Fermi surface should give rise to the redistribution of low-frequency spectral weight. In contradiction to this expectation, we do not find any significant change in the normal-state curve as temperature is reduced, other than the already mentioned shift to lower energies. In contrast, the $N_{\rm eff}(\omega, T)$ curve for the superconducting state does indeed show a reduction of spectral weight compared to the normal state. The missing area in $\sigma_1(\omega, T)$ in the superconducting state appears in a δ-function at $\omega = 0$, and this contribution is not included in the numerical integration which yields $N_{\rm eff}(\omega, T)$. Therefore, the difference between $N_{\rm eff}(\omega, T)$ above and below T_c is a measure of the strength of the δ function, and is proportional to the spectral weight in the superfluid condensate.

4.2. Dielectric function models

In analysing the *ab*-plane optical spectra of high-T_c materials, there has been much discussion over the one-component and the two-component pictures used to describe the optical conductivity [43]. In the two-component analysis, there are assumed to be two carrier types: free carriers which are responsible for the dc conductivity and which condense to form the superfluid below T_c, and bound carriers which dominate the mid-infrared region. Thus, the $\sigma_1(\omega)$ spectrum is decomposed into a Drude peak at $\omega = 0$ with a temperature-dependent scattering rate and a broad mid-infrared absorption band centred at finite frequencies, which is essentially temperature independent. An example of this approach is to fit the data to a Drude–Lorentz dielectric function

$$\epsilon(\omega) = -\frac{\omega_{pD}^2}{\omega^2 + \mathrm{i}\omega/\tau_D} + \sum_{j=1}^{N} \frac{\omega_{pj}^2}{\omega_j^2 - \omega^2 - \mathrm{i}\omega\gamma_j} + \epsilon_\infty \tag{2}$$

where ω_{pD} and $1/\tau_D$ are the plasma frequency and the scattering rate of the Drude component; ω_j, γ_j and ω_{pj} are the frequency, damping and oscillator strength of the jth Lorentzian contribution and ϵ_∞ is the high-frequency limit of $\epsilon(\omega)$ which includes interband transitions at frequencies above the measured range.

The alternative, a one-component picture, has only a single type of carrier; the difference between mid- and far-infrared response is attributed to a frequency dependence of the scattering rate and effective mass. As an empirical approach one can use the generalized Drude formalism

$$\epsilon(\omega) = \epsilon_\infty - \frac{\omega_p^2}{\omega(\omega + \mathrm{i}\gamma(\omega))} \tag{3}$$

where ω_p is the bare plasma frequency of the charge carriers, and $\gamma(\omega) = 1/\tau(\omega) - \mathrm{i}\omega\lambda(\omega)$ is the complex memory function. The quantities $1/\tau(\omega)$ and $\lambda(\omega)$ describe the frequency-dependent (unrenormalized) carrier scattering rate and mass enhancement so that the effective mass is given by $m^*(\omega) = m(1 + \lambda(\omega))$.

A one-component model also comes from the ideas of non-Fermi-liquid behaviour of the high-T_c superconductors, as introduced by Varma *et al* [26, 27] in the 'marginal Fermi liquid (MFL)' theory and Virosztek and Ruvalds [44, 45] in the 'nested Fermi liquid (NFL)' theory.

In the MFL theory, the dielectric function is

$$\epsilon(\omega) = \epsilon_\infty - \frac{\omega_p^2}{\omega[\omega - 2\Sigma(\omega/2)]} \tag{4}$$

where $\Sigma(\omega)$ represents the complex self-energy of the quasiparticles, and the factors of two arise because quasiparticle excitations come in pairs. The real part of Σ is related to the effective mass m^* by $m^*(\omega)/m = 1 - 2\,\mathrm{Re}\,\Sigma(\omega/2)/\omega$ whereas the imaginary part of Σ is related to the quasiparticle lifetime through $1/\tau^*(\omega) = -2m\mathrm{Im}\,\Sigma(\omega/2)/m^*(\omega)$.

The basic assumption of these theories is that there exists an anomalous charge or spin response (or both) for the cuprates. It is worth mentioning that other microscopic theories, such as the 'nearly antiferromagnetic Fermi liquid (NAFL)' theory proposed by Monthoux and Pines [46] and the 'phase-separation model' advocated by Emery and Kivelson [47], all lead to a similar picture. The self-energy, Σ, of the charge carriers (essentially the scattering rate) should take the form

$$-\mathrm{Im}\,\Sigma(\omega) \sim \begin{cases} \pi^2\lambda_T T & \omega < T \\ \pi\lambda_\omega\omega & \omega > T \end{cases} \tag{5}$$

where λ_T or λ_ω is a dimensionless coupling constant. Hence, for $\omega < T$ the model predicts a renormalized scattering rate that is linear in temperature, which agrees with the linear temperature dependence in the resistivity that is observed in nearly all copper oxide superconductors. As ω increases, reaching a magnitude of the order of T, interaction of the charge carriers with a broad spectrum of excitations comes to dominate the response. This causes $-\mathrm{Im}\,\Sigma(\omega)$ to grow linearly with frequency, up to a cutoff frequency ω_c that is introduced in the model.

The functions $1/\tau(\omega)$, $m^*(\omega)/m$ and $-\mathrm{Im}\,\Sigma(\omega)$ etc can all be calculated from the Kramers–Kronig derived dielectric function. In doing these calculations, we have used the bare plasma frequency values of ω_p, calculated from the conductivity sum-rule analysis in equation (1) with integration of $\sigma_1(\omega)$ up to the charge-transfer band. The values of ϵ_∞ are obtained from fitting the low-frequency reflectance data below the charge transfer gap by using a Drude–Lorentz model. In the following section, we will discuss the behaviour of the quasiparticle scattering rate from these different points of view.

4.3. Quasiparticle scattering rate

4.3.1. Generalized Drude model. First, let us focus on the frequency-dependent scattering rate, shown in figure 9, extracted from the generalized Drude formalism using equation (3). Starting with the Bi2212 crystal with $T_c = 85$ K, we find that the room-temperature $1/\tau(\omega, T)$ is linear up to 2000 cm^{-1}. When the temperature is reduced from 300 to 200 K, the high-frequency part of $1/\tau(\omega, T)$ gently decreases and still exhibits nearly linear frequency dependence while below 800 cm^{-1} the scattering rate $1/\tau(\omega, T)$ falls faster than linearly. The suppression in $1/\tau(\omega, T)$ at low frequencies is clearly resolved at lower temperatures. A similar feature has been previously observed optically and even discussed in relation to a pseudogap state [23–25]. At 20 K, the low-frequency $1/\tau(\omega, T)$ drops more sharply, although to use a Drude formula in the superconducting state does not seem correct.

Upon decreasing the carrier density in Bi2212, $T_c = 40$, 35 K, the frequency- and temperature-dependent behaviour in $1/\tau(\omega, T)$ is more interesting. The absolute value of the 300 K $1/\tau(\omega, T)$ increases at high frequencies. Unlike the case of the nearly optimally doped Bi2212, a distinct suppression of $1/\tau(\omega, T)$ is observed over the whole temperature range. The position where $1/\tau(\omega, T)$ deviates from being linear in ω seems to move towards

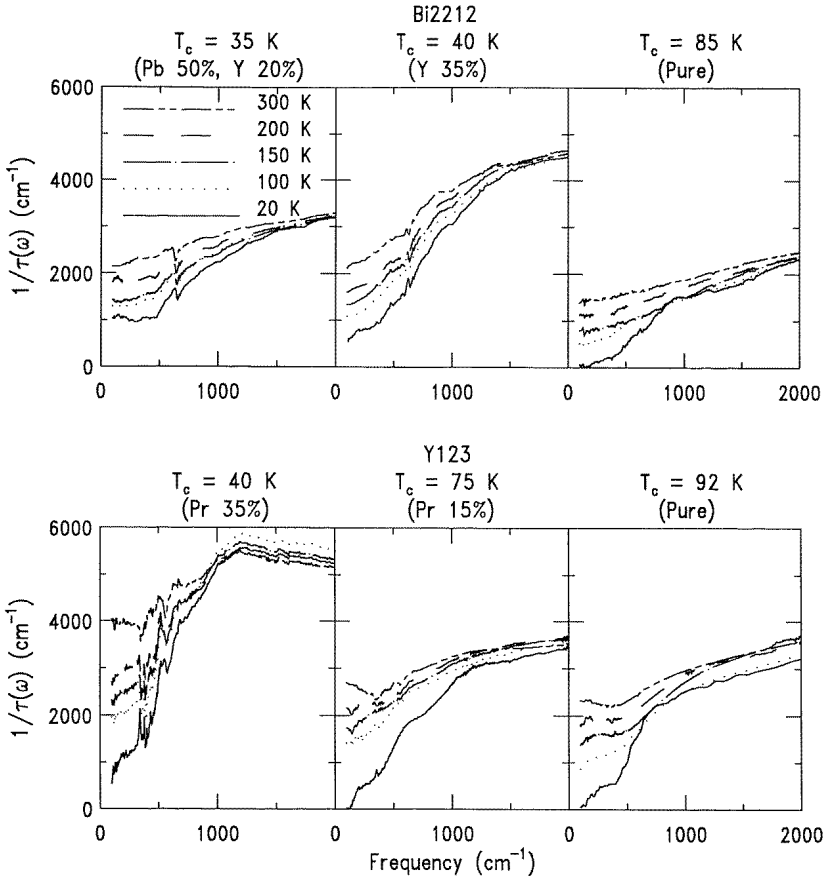

Figure 9. The temperature-dependent quasiparticle scattering rate $1/\tau(\omega, T)$ obtained from the generalized Drude model in equation (3) for $Bi_2Sr_2CaCu_2O_{8+\delta}$ and $YBa_2Cu_3O_{7-\delta}$ at several doping levels.

higher frequencies, and the depth of the normal-state threshold structure also increases as well. It is worthwhile to mention that above 1000 cm^{-1} the absolute value of the scattering rate in the Y 35%-doped Bi2212 is somewhat higher than that in the Pb 50%, Y 20%-doped sample. One possible explanation is that additional scattering mechanism, which originates from the *b*-axis superlattice structure of Bi2212, is removed by the Pb doping. Nevertheless, we would like to point out that the shape of the normal-state and superconducting-state $1/\tau(\omega, T)$ looks very similar in these heavily underdoped Bi2212s.

The $1/\tau(\omega, T)$ spectra for Y123 are shown in the lower panels of figure 9. We begin with the Y123 crystal with $T_c = 92$ K. At 300 K, the high-frequency $1/\tau(\omega, T)$ is approximately linear, with a deviation from linearity below 800 cm^{-1}. At lower frequencies we also observe a small upturn in the $1/\tau(\omega, T)$ spectra. Similar to the case of Bi2212, the scattering rate is suppressed more rapidly at low frequencies ($\omega < 800$ cm^{-1}) when temperature is reduced. Upon entering the superconducting state, the low-frequency $1/\tau(\omega, T)$ is depressed significantly. With 15% Pr substitution ($T_c = 75$ K), the overall magnitude of $1/\tau(\omega, T)$ is increased somewhat and the amount of change with temperature is diminished. In general,

$1/\tau(\omega, T)$ shows similar behaviour to the nearly optimally doped Y123. When the Pr content is increased to 35% ($T_c = 40$ K), the scattering rate is strongly enhanced at all frequencies. The frequency dependence of $1/\tau(\omega, T)$ is also modified as well. In particular, the slope of $1/\tau(\omega, T)$ becomes negative at higher frequencies, with a maximum near 1200 cm^{-1}. It is, moreover, remarkable that there is a resemblance in $1/\tau(\omega, T)$ between the spectra obtained at 20 K and at $T > T_c$.

4.3.2. Marginal Fermi liquid analysis. Figure 10 shows the imaginary part of the self-energy for various dopings and temperatures, calculated using the MFL formula in equation (4). For the nearly optimally doped Bi2212 and Y123, the 300 K $-\mathrm{Im}\,\Sigma(\omega, T)$ spectra increase with frequency in a quasilinear fashion though a small deviation from linearity below 400 cm^{-1} is observed in Y123. As the temperature is lowered, a threshold structure develops at low frequencies and becomes progressively steeper with the decrease of temperature while the temperature dependence is rather small in the high-frequency part of $-\mathrm{Im}\,\Sigma(\omega, T)$. The difference between the room-temperature and the superconducting-state $-\mathrm{Im}\,\Sigma(\omega, T)$ is

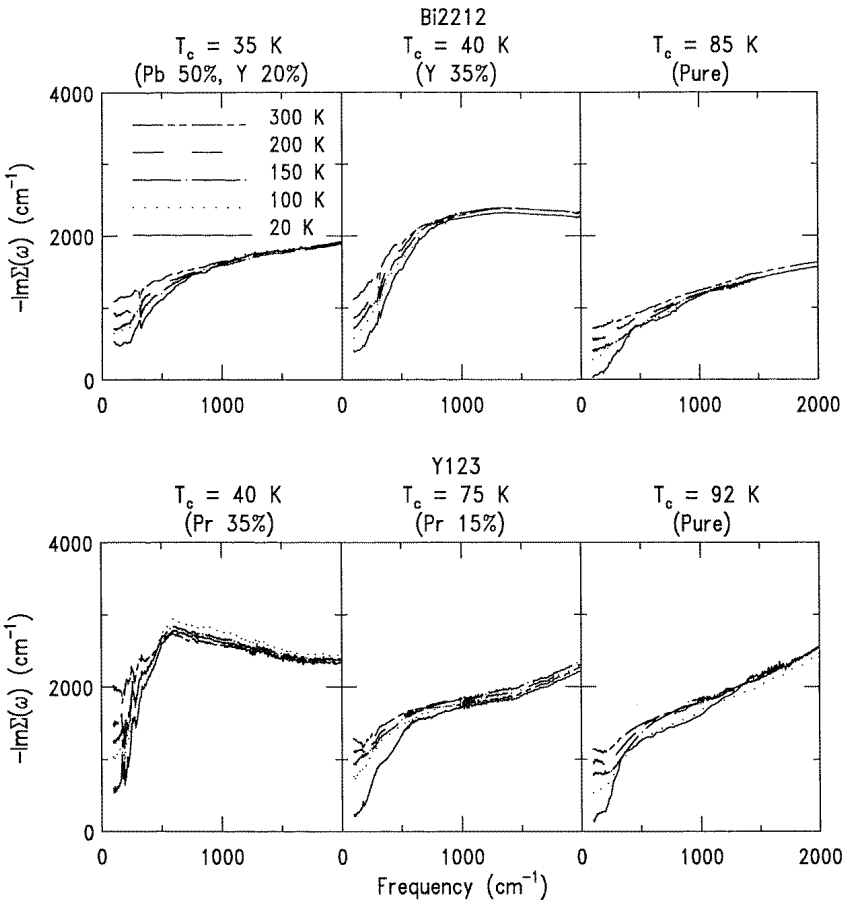

Figure 10. The imaginary part of the self-energy $-\mathrm{Im}\,\Sigma(\omega, T)$ obtained from the marginal Fermi liquid theory in equation (4) for various dopings and temperatures.

prominent at low frequencies. When carrier density is decreased, deviations from linear behaviour appear, even at room temperature; moreover, the shape of the normal-state $-\mathrm{Im}\,\Sigma(\omega, T)$ becomes similar to that in the superconducting state. It is important to note that the frequency scale associated with the suppression of $-\mathrm{Im}\,\Sigma(\omega, T)$ does change with doping. For most underdoped samples with $T_c = 35$, 40 K, the normal-state depression of $-\mathrm{Im}\,\Sigma(\omega, T)$ occurs at $\omega < 800$ cm^{-1}. As the doping level is increased towards the optimal, the onset frequency related to the changes of $-\mathrm{Im}\,\Sigma(\omega, T)$ is about 400 cm^{-1}.

Qualitatively, as shown in equation (5), there are two regimes to consider for the $-\mathrm{Im}\,\Sigma(\omega, T)$ function, i.e. $\omega < T$ and $\omega > T$. We obtain the coupling constants $\lambda_T = 0.4 \pm 0.02$ and 0.5 ± 0.1 in the regime $\omega < T$ for the nearly optimally doped Bi2212 and Y123. Furthermore, from evaluation of the slopes in the region where $-\mathrm{Im}\,\Sigma(\omega, T)$ is linear in ω, it is found that at 300 K $\lambda_\omega = 0.20 \pm 0.01$ in Bi2212 and $\lambda_\omega = 0.26 \pm 0.05$ in Y123. At 100 K these numbers are a factor of two larger. Note that our data are linear only below the cutoff frequency $\omega_c = 1200$ cm^{-1}. Much more interesting are the data for the underdoped crystals. The experimental $-\mathrm{Im}\,\Sigma(\omega, T)$ curves level off above ω_c, but below ω_c the slope is still larger than for the optimally doped specimens. In this respect, it appears that lowering the temperature of the sample would be equivalent to reducing the carrier density and, hence, to increase the coupling constant. Nevertheless, in accord with previous measurements on oxygen deficient Y123 single crystals [39], there is an increase in the quasiparticle interaction strength λ_ω with decreasing carrier concentration. These results are difficult to understand within an MFL perspective, because they imply that the lower-T_c materials have a larger λ_ω. The difficulty comes because T_c is also supposed to be determined by λ_ω. Thus, strong coupling means larger λ_ω and it should give rise to higher T_c. Finally, it is important to recall that the energy scale associated with the principal features in the $-\mathrm{Im}\,\Sigma(\omega, T)$ spectra obtained from the MFL analysis are all about half the value in the $1/\tau(\omega, T)$ spectra by using the generalized Drude approach. This factor occurs because the MFL theory assumes the quasiparticle excitation occurring in pairs, whereas a single excitation, such as a phonon or magnon, is assumed in the generalized Drude model.

4.3.3. Two-component picture. A completely different point of view is taken by the two-component picture. In this analysis, we have to subtract the mid-infrared absorption to obtain the Drude term or to fit to a combination of Drude and Lorentzian oscillators, given in equation (2). Figure 11 shows the zero-frequency scattering rate of the free-carrier or Drude contributions as a function of temperature from such an analysis. When $T > T_c$, $1/\tau_D$ varies linearly with temperature (together with an essentially temperature-independent Drude oscillator strength) for all doping levels studied. Such a temperature-linear behaviour in $1/\tau_D$ above T_c was observed earlier in the optimally doped cuprates [48–50]. We write $\overline{h}/\tau_D = 2\pi\lambda_D k_B T + \overline{h}/\tau_0$ [51], where λ_D is the dimensionless coupling constant that couples the charge carriers to the temperature-dependent excitations responsible for the scattering, and show in table 1, the values of ω_{pD}, λ_D and $1/\tau_0$. All the samples show a normal-state $1/\tau_D$ linear in T, with all about the same slope, giving $\lambda_D \sim 0.2$–0.3. The fit is shown as the solid line. This is remarkable: despite the huge difference in T_c, the coupling constant λ_D is the same in these materials. They differ only in their intercept, which is a measure of the residual resistivity of each sample. The residual resistivity can also be seen in the data in figure 1. Below T_c, $1/\tau_D$ in all studied samples shows a quick drop from T-linear behaviour, which has been pointed out previously in the optimally doped regime [49, 50]. More recently, a similar fast drop in $1/\tau_D$ was also found in Pr-doped and oxygen-reduced Y123 films using terahertz coherent time-domain spectroscopy [52, 53]. This striking feature seems to be a unique property of the cuprates. It is noteworthy that the low-temperature values of $1/\tau_D$

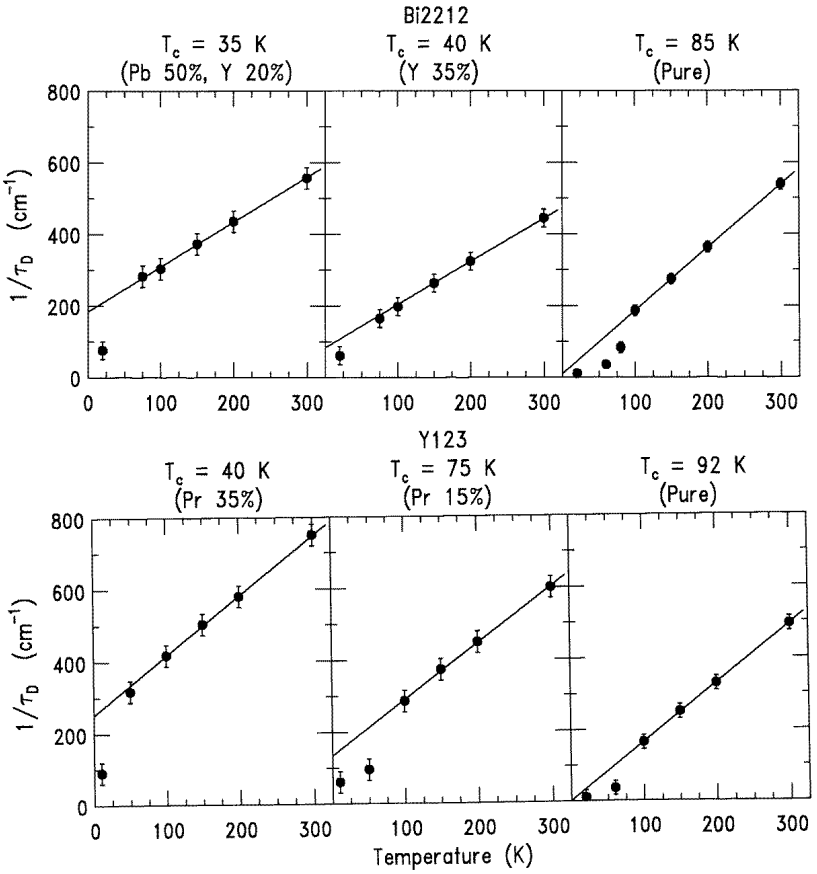

Figure 11. The zero-frequency scattering rate $1/\tau_D$ of the Drude contribution from the two-component fit of equation (2) to the optical conductivity. The straight lines show a linear fit to the temperature dependence of $1/\tau_D$ above T_c.

approach zero in the optimally doped samples as T is lowered. Although $1/\tau_D$ does not go to zero at low T in the underdoped materials, it is smaller than the extrapolated intercept $1/\tau_0$ of the linear regime above T_c. This behaviour could imply that the superconducting-state quasiparticle scattering rate is governed by the impurity effects. Another viewpoint is based on the nodes (zeros) of the gap function, and then the scattering rate reflects the response of the quasiparticle states with small excitation energies.

4.3.4. Compare with dc transport. It is interesting to compare the scattering rate with the dc resistivity data. The most striking feature in figures 9 and 10 is that both the normal-state $1/\tau(\omega, T)$ and $-\mathrm{Im}\,\Sigma(\omega, T)$ spectra show a threshold structure at low frequencies in the underdoped materials. When the doping reaches the optimal level the threshold structure is weakened. The dc resistivity in figure 1 of underdoped crystals is a linear function in T for $T > T^*$, but shows a crossover to a steeper slope at $T < T^*$. If the temperature dependence of the normal-state resistivity $\rho = (m/ne^2)(1/\tau)$ is attributed entirely to the scattering rate, then the crossover behaviour could be attributed to the low-frequency suppression of the scattering rate. As discussed already, this view is further supported by many experimental observations

Table 1. Drude plasma frequency, ω_{pD}, coupling constant, λ_D, and the zero-temperature intercept, $1/\tau_0$, for six materials.

Materials	T_c (K)	ω_{pD} (cm^{-1})	λ_D	$1/\tau_0$ (cm^{-1})
$Bi_2Sr_2CaCu_2O_{8+\delta}$	85	9000 ± 200	0.28	9
Y 35%	40	5600 ± 200	0.20	85
Pb 50%, Y 20%	35	6100 ± 200	0.20	185
$YBa_2Cu_3O_{7-\delta}$	92	9800 ± 200	0.26	2
Pr 15%	75	8700 ± 200	0.25	135
Pr 35%	40	6800 ± 200	0.26	252

showing that the pseudogap state develops at $T < T^*$ in the underdoped compounds. However, in this connection we should remark on a discrepancy between the scattering rate and the pseudogap state. As shown in figures 9 and 10, it must be recognized that a threshold structure exists already at room temperature in the underdoped samples even though all dc resistivity curves exhibit a linear T dependence from 300 K to T^*. Moreover, when a pseudogap opens, the amount of low-energy scattering decreases, implying that the absolute value of the scattering rate in the sample must be lower than that without a pseudogap state. Our experimental observations are not in accord with this expectation. First, as shown in figure 11, the two-component analysis shows that the linear-T behaviour in $1/\tau_D$ was found in all samples. Second, the decreased scattering rate is nearly the same independent of whether the pseudogap is expected or not. Third, the limited number of points and possible uncertainties especially below 100 cm^{-1} prevent us from determining whether the observed deviation from linearity below T^* in dc resistivity data is consistent with our present results in $1/\tau_D$. However, a strong suppression in scattering, as suggested by the $1/\tau(\omega, T)$ and $-\mathrm{Im}\,\Sigma(\omega, T)$ results, is ruled out.

4.4. Superconducting response

4.4.1. Superconducting gap. The superconducting gap and the nature of the superconducting condensate are two fundamental quantities which characterize the superconducting state. An ordinary s-wave superconductor has a gap Δ in its excitation spectrum, which causes $\sigma_1(\omega)$ to be zero up to $\omega = 2\Delta$; above this frequency $\sigma_1(\omega)$ rises to join the normal-state conductivity [54]. Furthermore, structure in $\sigma_1(\omega)$ at $2\Delta + \Omega_0$ reflects peaks at Ω_0 in the effective phonon-mediated interaction $\alpha^2 F(\Omega)$, and a detailed measurement of $\sigma_1(\omega)$ can in principle determine $\alpha^2 F(\Omega)$ [55]. Thus it was hoped that infrared measurements of $\sigma_1(\omega)$ for the high-T_c superconductors would provide similar information on both the gap and the pairing mechanism. However, in spite of a considerable number of data on high-quality samples, there is no consensus yet whether a superconducting gap is observable in the infrared spectrum. For several reasons, the search for evidence of a superconducting gap in high-T_c materials has proven difficult.

First, gap anisotropy can lead to broadening of the absorption edge and a diminution of the gap structure in the optical conductivity. ARPES of Bi2212 implies that the gap is highly anisotropic in k-space. The corresponding optical conductivity spectrum would not exhibit a sharp onset. Second, if one interprets the $\sigma_1(\omega)$ data based on the two-component model as described in equation (2), then the presence of the second component (mid-infrared band) can overlap and possibly mask any gap absorption. In this view the quasiparticle scattering rate may be low relative to the superconducting energy gap ($1/\tau_D \ll 2\Delta$) so that one is in the clean limit in which almost all of the free carriers condense to form the superfluid and little spectral

weight is left for transition across the gap. In principle, one can experimentally test the second point by enhancing the scattering rate to produce optimum circumstances for the observation of the 2Δ onset in $\sigma_1(\omega)$. Doping is an important method to study this possibility.

As shown in figure 4, the superconducting-state conductivity of the nearly optimally doped samples is finite and no superconducting gap exists down to the low-frequency limit of our measurements, consistent with previous reflectance [56, 57] and direct absorption data [58]. The finite absorption in the superconducting state is not due to experimental problems or sample-to-sample variation, suggesting that it is a fundamental characteristic of the fully doped materials. One of the possible origins is the tail of the mid-infrared absorption in the two-component model. The other possibility could be associated with nodes in the superconducting gap, such as might occur in the d-wave superconductor [59, 60]. For the most underdoped Bi2212 crystal ($T_c = 35$ K), shown in figure 7, there is no evidence of a gap in the superconducting spectra. The effect of doping on the optical absorption spectrum in the gap region does not produce dirty-limit behaviour as seen in conventional superconductors—an onset of absorption at 2Δ. Instead, a new low-frequency, Drude-like, absorption appears in the superconducting state, taking spectral weight away from the superconducting condensate. This observation could be also due to the unconventional nature of the response of the high-T_c superconductors. If a d-wave gap is a possible scenario, the low-frequency absorption will be enhanced in a dirty sample.

4.4.2. Superfluid density. Although there is still a lot of controversy about the experimental data and their interpretations regarding optical studies of the superconducting gap in the cuprates, the spectral weight or oscillator strength of the superconducting condensate is given less ambiguously from infrared measurements. A superconductor has a low-frequency $\sigma_1(\omega)$ that is a δ-function at $\omega = 0$; in turn, this δ-function gives (by Kramers–Kronig) a contribution to $\epsilon_1(\omega)$ of $\epsilon_1(\omega) = \epsilon_\infty - \omega_{pS}^2/\omega^2$. Thus the ω^2 component of the very low-frequency $\epsilon_1(\omega)$ measures the superfluid density directly and is equivalent to a penetration depth λ_L experiment. Figure 12 shows $\epsilon_1(\omega)$ plotted against ω^{-2}; a linear regression of the straight line yields ω_{pS}. Results for all our samples are listed in table 2.

Table 2. Plasma frequency of the condensate, ω_{pS}, and the penetration depth, λ_L, at 20 K.

Materials	T_c (K)	ω_{pS} (cm^{-1})	λ_L (Å)
$Bi_2Sr_2CaCu_2O_{8+\delta}$	85	8800 ± 200	1860
Y 35%	40	4100 ± 400	4130
Pb 50%, Y 20%	35	3700 ± 400	4910
$YBa_2Cu_3O_{7-\delta}$	92	9200 ± 200	1720
Pr 15%	75	7700 ± 400	2110
Pr 35%	40	4200 ± 400	4260

The superconducting penetration depth is a related parameter, which we are naturally led to associate with the superfluid density. It is a direct measure of the density of carriers n_s condensed in the superconducting state and through its temperature dependence, the symmetry of the superconducting order parameter can be discriminated. The penetration depth is usually determined by experiments of muon spin rotation (μSR), DC magnetization and surface impedance in the microwave and millimetre wavelength region. The latter two methods, while they yield the temperature dependence of the penetration depth with great accuracy, generally cannot be used to obtain its absolute value. In the case of infrared measurements, the penetration depth can be found from Kramers–Kronig analysis of the reflectance data, which

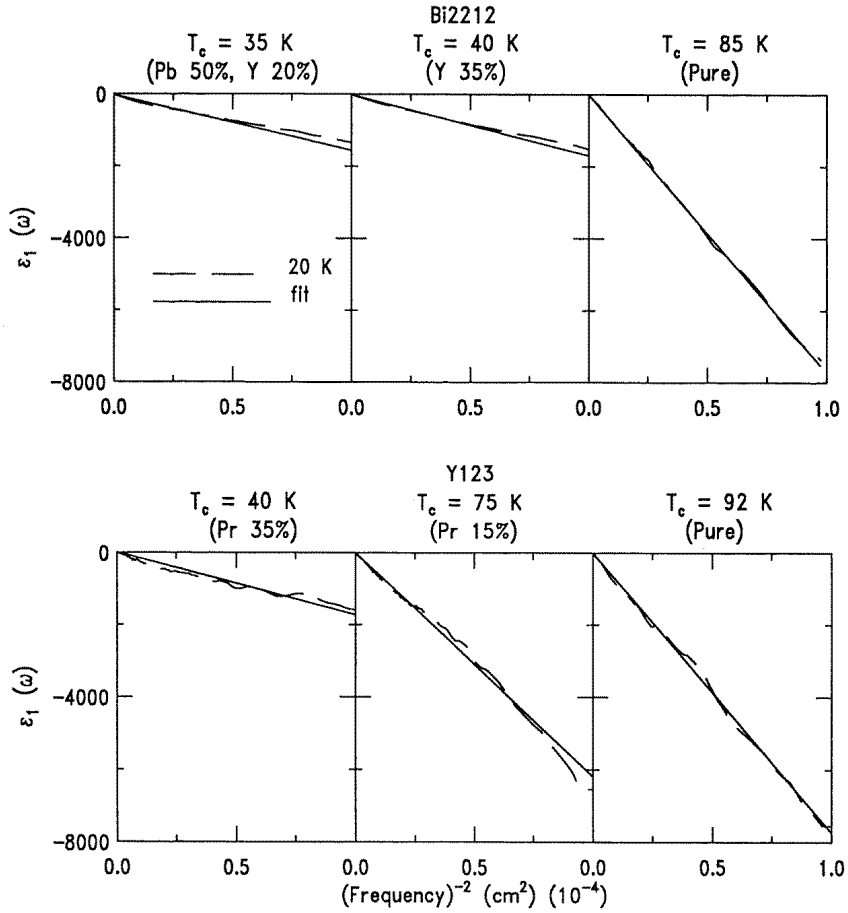

Figure 12. The real part of the dielectric function (dashed line), plotted against ω^{-2} at 20 K. The range of the data shown is 500–100 cm^{-1}. The linear fits are shown by the solid lines.

gives the imaginary part $\sigma_2(\omega)$ of the complex conductivity as well as the real part $\sigma_1(\omega)$. $\sigma_2(\omega)$ is directly related to a generalized $\lambda_L(\omega)$:

$$\lambda_L(\omega) = \left[\frac{c^2}{4\pi\omega\sigma_2(\omega)}\right]^{1/2} \tag{6}$$

where c is the light speed. Equation (6) is a direct consequence of the δ-function in the real part of the conductivity at $\omega = 0$. The frequency-dependent penetration depth of all the samples at 20 K is shown in figure 13. Note that a smaller λ_L corresponds to a larger superfluid density. $\lambda_L(\omega)$ is almost frequency independent at low temperatures in the samples near optimal doping, suggesting that the superfluid response dominates the other contributions to the conductivity. In contrast, for the underdoped compounds, $\lambda_L(\omega)$ shows some frequency dependence below 300 cm^{-1}, an indication that not all of the free carriers have condensed into the δ-function.

Alternatively, the conductivity sum rule provides a good estimate for the strength of the δ-function peak,

$$\frac{c^2}{\lambda_L^2(0)} = 8\int_0^\infty (\sigma_{1n}(\omega) - \sigma_{1s}(\omega))\,\mathrm{d}\omega \tag{7}$$

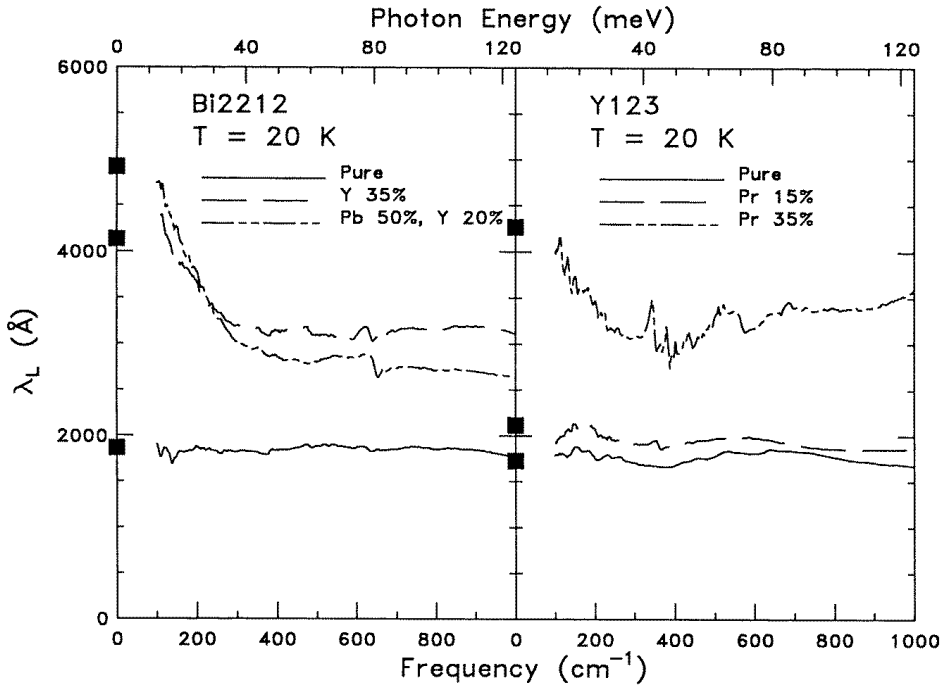

Figure 13. The frequency-dependent superconducting penetration depth $\lambda_L(\omega)$ obtained from equation (6) at 20 K. The values of $\lambda_L(0)$ from the sum-rule analysis of equation (7) are indicated by the symbols.

where $\sigma_{1n}(\omega)$ and $\sigma_{1s}(\omega)$ are the real parts of the complex conductivity at $T \approx T_c$ and $T \ll T_c$, respectively. Equation (7) states the spectral weight lost at low frequencies in the superconducting state has been transferred to the zero-frequency δ-function response of the superconducting condensate. This missing spectral weight from the sum rule is indicated by solid squares in figure 13. The values of penetration depth of all samples obtained by equation (7) are displayed in table 2. Generally speaking the two estimates for λ_L in equations (6) and (7) agree within about 10%. The penetration depth is related to the plasma frequency of the condensate by $\lambda_L = c/\omega_{pS}$. The values of ω_{pS} obtained directly from the dielectric function $\epsilon_1(\omega)$ or through the sum rule agree well.

4.4.3. Spectral weight above and below T_c. We now turn to a comparison among the various contributions to $\sigma_1(\omega)$, above and below T_c. We have used finite-frequency sum-rule analysis in equation (1) and then calculated the effective number of carriers per planar Cu atom in the low-frequency region below the charge-transfer gap as $N_{\rm tot}$, the Drude or free-carrier part (from two-component analysis) as $N_{\rm Drude}$ and the superconducting condensate weight as $N_{\rm s}$. Results for our Bi2212 and Y123 systems together with oxygen-doped $La_2CuO_{4.12}$ [61] (La214(O)) and fully optimal $Tl_2Ba_2CaCu_2O_8$ [62] (Tl2212) are summarized in table 3. $N_{\rm s}$ is also shown as a fraction of $N_{\rm tot}$ and $N_{\rm Drude}$. Notably, there is an 'universal correlation' between the numbers of carriers and the transition temperature. This correlation holds whether one considers the number of carriers in the superfluid or the total number of carriers. In figure 14 we plot T_c versus $n_{\rm tot}$ for high-T_c superconductors, where $n_{\rm tot} = N_{\rm tot} \cdot N_{\rm Cu}/V_{\rm cell}$ [63]. One Bi2212 sample has $T_c = 68$ K by Ni 2.15% substitution [64]. In addition, one point has also been

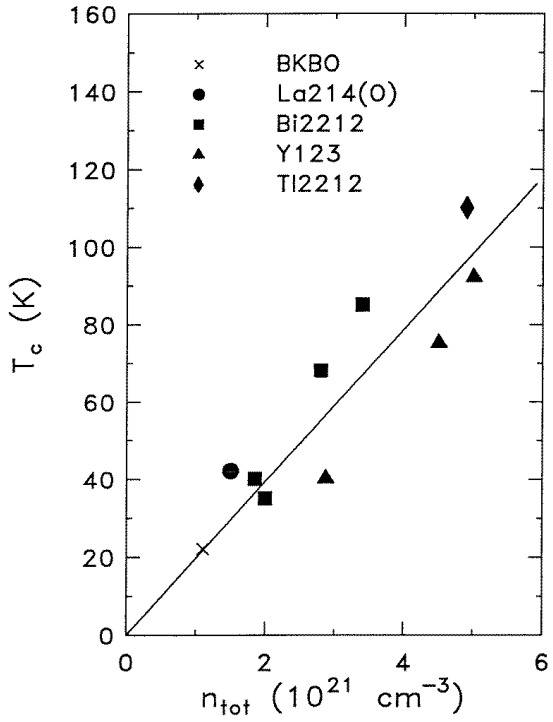

Figure 14. The transition temperature T_c as a function of $n_{\rm tot}$ for $Ba_{1-x}K_xBiO_3$ (cross) [65], $La_2CuO_{4.12}$ (circle) [61], $Bi_2Sr_2CaCu_2O_{8+\delta}$ (square), $YBa_2Cu_3O_{7-\delta}$ (triangle) and $Tl_2Ba_2CaCu_2O_8$ (diamond) [62]. The solid line is a guide to the eye.

included for a superconductor oxide that is not based on CuO_2 planes, $Ba_{1-x}K_xBiO_3$ (BKBO) with $T_c = 28$ K [65]. All of the data points follow an approximately common line. In the conventional superconductors an increased carrier density normally leads to an increased T_c. A similar trend has been observed for the cuprates at the doping level in the underdoped and optimal doped regime. Interestingly, a recent study [66] on the optical conductivity of high-T_c superconductors from the underdoped to overdoped range points out that in the underdoped regime progressive doping indeed increases the low-frequency conductivity spectral weight while this trend does not continue to the overdoped part of the phase diagram. It is argued that there is an increase in the carrier density as T_c is increasing, and overdoping decreases T_c but does not lead to an increase in the total number of carriers. Another important point from the values of $N_{\rm tot}$ is that in a simple rigid-band picture, the total number of doping carriers corresponds to the volume enclosed by the Fermi surface. This interpretation, however, runs into a discrepancy between optical and photoemission determinations of carrier number. Recent ARPES measurements of Bi2212 [67] ranging from underdoped to overdoped imply a large Luttinger Fermi surface, consistent with $N_{\rm tot} = 1+x$ where x is the dopant concentration. In contrast, optical measurements imply that $N_{\rm tot} = x$ and we always see a small Fermi surface for all doping levels studied.

Figure 15 shows the relation between T_c and $n_{\rm s}$, where $n_{\rm s} = N_{\rm s} \cdot N_{\rm Cu}/V_{\rm cell}$ [63]. The most striking finding in the plot is that for the underdoped and optimally doped cuprates (filled symbols) the superfluid density increases roughly proportionally to the transition temperature. Our optical data points follow what is generally referred to as the Uemura line. These results

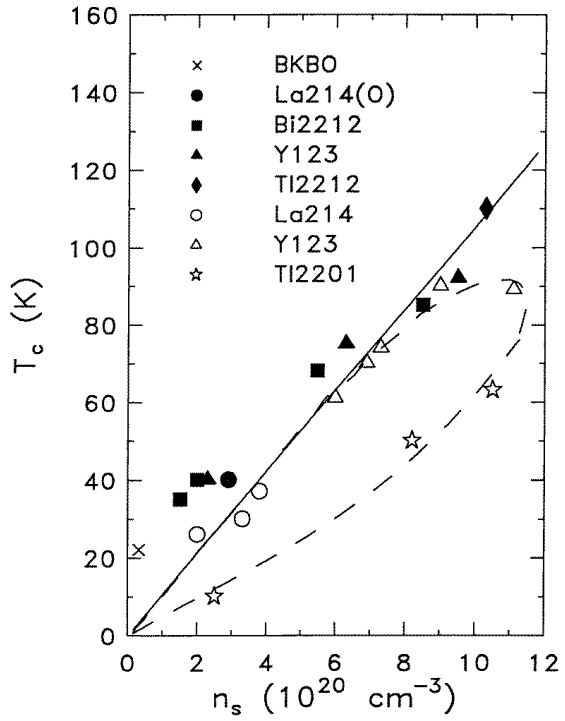

Figure 15. T_c plotted a function of n_s. Cross: $Ba_{1-x}K_xBiO_3$ [65], filled circle: $La_2CuO_{4.12}$ [61], filled square: $Bi_2Sr_2CaCu_2O_{8+\delta}$, filled triangle: $YBa_2Cu_3O_{7-\delta}$ and filled diamond: $Tl_2Ba_2CaCu_2O_8$ [62] from infrared measurements. Open circle: $La_{2-x}Sr_xCuO_4$, open triangle: $YBa_2Cu_3O_{7-\delta}$ and open star: $Tl_2Ba_2CuO_6$ from μSR measurements [68–71]. The solid curve is the universal Uemura line [68]. The dashed curve is based on a pair-breaking model calculation [71].

Table 3. Effective number of carriers per planar Cu atom.

Materials	T_c (K)	$N_{\rm tot}$	$N_{\rm Drude}$	$N_{\rm s}$	$\frac{N_{\rm s}}{N_{\rm tot}}$ (%)	$\frac{N_{\rm s}}{N_{\rm Drude}}$ (%)
$La_2CuO_{4.12}$	40	0.14	0.035	0.028	20	80
$Bi_2Sr_2CaCu_2O_{8+\delta}$	85	0.38	0.105	0.092	24	88
Y 35%	40	0.21	0.04	0.02	8	50
Pb 50%, Y 20%	35	0.23	0.05	0.017	7	34
$YBa_2Cu_3O_{7-\delta}$	92	0.44	0.093	0.082	19	89
Pr 15%	75	0.375	0.073	0.054	14	74
Pr 35%	40	0.25	0.045	0.02	8	44
$Tl_2Ba_2CaCu_2O_8$	110	0.54	0.13	0.115	21	88
Typical uncertainties	±2	±0.03	±0.01	±0.01	±1%	±4%

suggest that, regardless of charge or impurity doping, it is the parameter n_s that determines T_c of the cuprate superconductors. As is well known from the μSR measurements (open symbols), there is a 'universal correlation' between T_c and n_s in many cuprate superconductors: T_c increases linearly with n_s (solid line) with increasing carrier doping in the underdoped region, then shows saturation in the optimum-T_c region [68, 69]. In the overdoped $Tl_2Ba_2CuO_6$ (Tl2201) systems, both T_c and n_s decrease (dashed line) with increasing hole doping [70, 71],

bringing the trajectory in T_c versus n_s back to the origin. We are presently unaware of any optical analysis on the evolution of superfluid density in the overdoped cuprates, so this subject will be addressed in future work. Finally, considering the superconducting condensate fraction in table 3, we find that in all optimally doped materials, about 20–25% of the total doping carriers joins the superfluid; about 75–80% remains at finite frequencies. Furthermore, if a two-component picture is adopted, then nearly 90% of the free-carrier spectral weight condenses. In other words, the oscillator strength of the δ-function is essentially the same as the Drude-like peak of the normal state, which is a clean-limit point of view. These results also indicate that the large portion of spectral weight in the normal state condenses below T_c in the optimally doped samples, while the superconducting condensate in the underdoped materials is rather small.

5. Summary

In summary, the *ab*-plane optical reflectances of single crystals of Bi2212 and Y123 were measured over a wide frequency and temperature range. Substitution of Y for Ca atoms in Bi2212 and Pr for Y atoms in Y123 allowed us to study the doping range from heavily underdoped to nearly optimally doped. We have examined a variety of spectral functions from Kramers–Kronig analysis of the reflectance data. With the reduction of carrier concentration in the CuO_2 planes, we observe there is a lot of spectral weight lost in the infrared conductivity. The weight lost below the charge-transfer absorption band is transferred to higher frequencies. We present a complete spectral investigation of the most underdoped Bi2212 with $T_c = 35$ K. Emphasis has been placed on the features in the real part of the conductivity $\sigma_1(\omega, T)$ and the development of the spectral weight $N_{\rm eff}(\omega, T)$, as the temperature of sample changes from above T^* to below the critical temperature T_c. We find that the conductivity below 300–400 $\rm cm^{-1}$ is approximately Drude-like, a zero-frequency peak which grows and sharpens as temperature is reduced. At the same time, the spectral weight associated with the free carriers shifts to lower frequencies. It is difficult to relate our experimental observations to the normal-state pseudogap phenomenon.

Considering the important role that quasiparticle damping has played in discerning the normal-state pseudogap features, we derive the scattering rate from both the one-component and the two-component pictures. In one-component analysis, our results were treated within the framework of the generalized Drude model and the marginal Fermi liquid theory [26, 27]. The appearance of low-frequency depression in the scattering rate spectrum (from previous measurements [23–25] as well as those reported here) signals entry into the pseudogap state. The energy scale associated with the principal features in $1/\tau(\omega, T)$ and $-\mathrm{Im}\,\Sigma(\omega, T)$ shows a factor of two difference. The frequency scale associated with the suppression of $-\mathrm{Im}\,\Sigma(\omega, T)$ does change with doping. For the most underdoped samples with $T_c = 35$, 40 K, the normal-state depression of $-\mathrm{Im}\,\Sigma(\omega, T)$ occurs at $\omega < 800$ $\rm cm^{-1}$. As the doping level is increased towards the optimal, the onset frequency related to the changes of $-\mathrm{Im}\,\Sigma(\omega, T)$ was found to be 400 $\rm cm^{-1}$. An alternative approach is to consider the zero-frequency $1/\tau_D$ from free-carrier contributions. We find that for all the samples studied, when $T > T_c$, $1/\tau_D$ varies linearly with temperature and decreases quickly below T_c. $1/\tau_D$ from inelastic scattering process puts all the samples in the weak-coupling limit ($\lambda_D \sim 0.2$–0.3). We suggest that the pronounced features in the scattering rate spectrum are related to the manner in which the data are analysed (one versus two components). It is a delicate question to ask which analysis, one component or two component, is more appropriated in our present study [72].

In the superconducting state, some of the finite-frequency oscillator strength in $\sigma_1(\omega)$ is removed by the superconducting transition. A finite low-lying conductivity remains below T_c. There is no convincing evidence of superconducting gap absorption in our spectra. In

the case of the materials with near optimal doping, the absence of a superconducting gap can be explained in one of two ways: a clean-limit picture in the two-component model or the presence of an unconventional gap with nodes somewhere on the Fermi surface. However, our underdoped (dirtier) samples again show no sign of a gap, which favours the latter argument. In determining the amount of oscillator strength that condenses into the δ-function at $\omega = 0$, we obtain a good agreement of the values of superfluid density from the missing area by the sum-rule argument with ω_{pS}, or through the superconducting penetration depth λ_L. The spectral weight lost at low frequencies in the superconducting state is large in the nearly optimally doped samples; a sum-rule evaluation finds that about 20–25% of the total doping-induced carriers in is the δ-function. In contrast, in the most underdoped samples the superfluid density is very small. We also find that there is a 'universal correlation' between the numbers of carriers and the transition temperature. This correlation holds whether one considers the number of carriers in the superfluid or the total number of carriers. Our optical results are significant and consistent with the evidence from μSR measurements: T_c scales linearly with n_s in many underdoped and optimally doped cuprates.

Acknowledgments

Research is supported at the University of Florida by National Science Foundation (NSF) grant No DMR-9705108, at the National High Magnetic Field Laboratory by NSF cooperative agreement No DMR-9527035 and by the State of Florida, at Texas by NSF grant DMR-9158089 and at Wisconsin by NSF grant DMR-8911332.

References

[1] Levi B G 1996 *Phys. Today* **49** 7
[2] Warren W W Jr, Walstedt R E, Brennert G F, Cava R J, Tycko R, Bell R F and Dabbagh G 1989 *Phys. Rev. Lett.* **62** 1193
[3] Alloul H, Ohno T and Mendels P 1989 *Phys. Rev. Lett.* **63** 1700
[4] Yoshinari Y, Yasuoka H, Ueda Y, Koga K and Kosuge K 1990 *J. Phys. Soc. Japan* **59** 3698
[5] Takigawa M, Reyes A P, Hammel P C, Thompson J D, Heffner R H, Fisk Z and Ott K C 1991 *Phys. Rev.* B **43** 247
[6] Rossat-Nignod J, Regnault L P, Vettier C, Bourges P, Burlet P, Bossy J, Henry J Y and Lapertot G 1991 *Physica* C **185–189** 86
[7] Tranquada J M, Gehring P M, Shirane G, Shamoto S and Sato M 1992 *Phys. Rev.* B **46** 5561
[8] Loram J W, Mirza K A, Cooper J R and Liang W Y 1994 *Phys. Rev. Lett.* **71** 1740
[9] Bucher B, Steiner P, Karpinski J, Kaldis E and Wachter P 1993 *Phys. Rev. Lett.* **70** 2012
[10] Batlogg B, Hwang H Y, Takagim H, Cava R J, Kao H L and Kwo J 1994 *Physica* C **235–240** 130
[11] Ito T, Takenaka K and Uchida S 1993 *Phys. Rev. Lett.* **70** 3995
[12] Nemetschek R, Opel M, Hoffmann C, Müller P F, Hackl R, Berger H, Forró L, Erb A and Walker E 1997 *Phys. Rev. Lett.* **78** 4837
[13] Chen X K, Naeini J G, Hewitt K C, Irwin J C, Liang R and Hardy W N 1997 *Phys. Rev.* B **56** R513
[14] Blumberg G, Kang Moonsoo, Klein M V, Kadowaki K and Kendziora C 1997 *Science* **278** 1427
[15] Renner Ch, Revaz B, Genoud J-Y, Kadowaki K and Fischer O 1998 *Phys. Rev. Lett.* **80** 149
[16] Loeser A G, Dessau D S and Shen Z-X 1996 *Physica* C **263** 208
[17] Marshall D S *et al* 1996 *Phys. Rev. Lett.* **76** 4841
[18] Ding H, Yokoya T, Campuzano J C, Takahashi T, Randeria M, Norman M R, Mochiku T, Kadowaki K and Giapintzakis J 1996 *Nature* **382** 51
[19] Norman M R *et al* 1998 *Nature* **392** 157
[20] Homes C C, Timusk T, Liang R, Bonn D A and Hardy W N 1993 *Phys. Rev. Lett.* **71** 1645
[21] Homes C C, Timusk T, Bonn D A, Liang R and Hardy W N 1995 *Physica* C **254** 265
[22] Basov D N, Timusk T, Dabrowski B and Jorgensen J D 1994 *Phys. Rev.* B **50** 3511
[23] Puchkov A V, Fournier P, Basov D N, Timusk T, Kapitulnik A and Kolesnikov N N 1996 *Phys. Rev. Lett.* **77** 3212

[24] Basov D N, Liang R, Dabrowski B, Bonn D A, Hardy W N and Timusk T 1996 *Phys. Rev. Lett.* **77** 4090
[25] Puchkov A V, Basov D N and Timusk T 1996 *J. Phys.: Condens. Matter* **8** 10 049
[26] Varma C M, Littlewood P B, Schmitt-rink S, Abrahams E and Ruckenstein A E 1989 *Phys. Rev. Lett.* **63** 1996
[27] Littlewood P B and Varma C M 1991 *J. Appl. Phys.* **69** 4979
[28] Tamegai T, Koga K, Suzuki K, Ichihara M, Sakai F and Iye Y 1989 *Japan. J. Appl. Phys.* **28** L112
[29] Wang N L, Buschinger B, Geibel C and Steglich F 1996 *Phys. Rev.* B **54** 7445
[30] Takenaka K, Imanaka Y, Tamasaku K, Ito T and Uchida S 1992 *Phys. Rev.* B **46** 5833
[31] Paulius L M, Lee B W, Maple M B and Tsai P K 1994 *Physica* C **230** 255
[32] Takagi H, Batlogg B, Kao H L, Kwo J, Cava R J, Krajewski J J and Peck W F Jr 1992 *Phys. Rev. Lett.* **69** 2975
[33] Nakamura Y and Uchida S 1993 *Phys. Rev.* B **47** 8369
[34] Tajima S *et al* 1989 *J. Opt. Soc. Am.* B **6** 475
[35] Koch B, Geserich H P and Wolf T 1989 *Solid State Commun.* **71** 495
[36] Wooten F 1972 *Optical Properties of Solids* (New York: Academic)
[37] Uchida S, Ido T, Takagi H, Arima T and Tokura Y 1991 *Phys. Rev.* B **43** 7942
[38] Orenstein J, Thomas G A, Millis A J, Cooper S L, Rapkine D H, Timusk T, Schneemeyer L F and Waszczak J V 1990 *Phys. Rev.* B **42** 6342
[39] Cooper S L, Reznik D, Kotz A, Karlov M A, Liu R, Klein M V, Lee W C, Giapintzakis J and Ginsberg D M 1993 *Phys. Rev.* B **47** 8233
[40] Tinkham M and Ferrell R A 1959 *Phys. Rev. Lett.* **2** 331
[41] Litvinchuk A P, Thomsen C and Cardona M 1993 *Physical Properties of High Temperature Superconductors IV* ed D M Ginsberg (Singapore: World Scientific) p 375
[42] Egami T and Billinge S J L 1995 *Physical Properties of High Temperature Superconductors V* ed D M Ginsberg (Singapore: World Scientific) p 265
[43] Tanner D B and Timusk T 1992 *Physical Properties of High Temperature Superconductors III* ed D M Ginsberg (Singapore: World Scientific) p 363
[44] Virosztek A and Ruvalds J 1990 *Phys. Rev.* B **42** 4064
[45] Rieck C T, Little W A, Ruvald J and Virosztek A 1995 *Phys. Rev.* B **51** 3772
[46] Monthoux P and Pines D 1994 *Phys. Rev.* B **49** 4261
[47] Emery V J, Kivelson S A and Liu H Q 1990 *Phys. Rev. Lett.* **64** 475
Emery V J and Kivelson S A 1993 *Physica* C **209** 597
[48] Kamarás K *et al* 1990 *Phys. Rev. Lett.* **64** 84
[49] Romero D B, Porter C D, Tanner D B, Forro L, Mandrus D, Mihaly L, Carr G L and William G P 1992 *Phys. Rev. Lett.* **68** 1590
[50] Gao F, Romero D B, Tanner D B, Talvacchio J and Forrester M G 1993 *Phys. Rev.* B **47** 1036
[51] Allen P B, Beaulac T P, Khan F S, Butler W H, Pinski F J and Swihart J C 1986 *Phys. Rev.* B **34** 4331
[52] Francois I *et al* 1996 *Phys. Rev.* B **53** 12 502
[53] Ludwig C, Jiang Q, Kuhl J and Zegenhagen J 1996 *Physica* C **269** 249
[54] Glover R E and Tinkham M 1956 *Phys. Rev.* B **107** 844
Glover R E and Tinkham M 1957 *Phys. Rev.* B **108** 243
[55] Brandi G and Sievers A J 1972 *Phys. Rev.* **5** 3350
[56] Quijada M A, Tanner D B, Kelley R J and Onellion M 1994 *Z. Phys.* B **94** 255
[57] Basov D N, Liang R, Bonn D A, Hardy W N, Dabrowski B, Quijada M, Tanner D B, Rice J P, Ginsberg D M and Timusk T 1995 *Phys. Rev. Lett.* **74** 598
[58] Pham T, Lee M W, Drew H D, Welp U and Fang Y 1991 *Phys. Rev.* B **44** 5377
[59] Hirschfeld P J, Putikka W O and Scalapino D J 1993 *Phys. Rev. Lett.* **71** 3705
[60] Scalapino D J 1995 *Phys. Rep.* **250** 329
[61] Quijada M A, Tanner D B, Chou F C, Johnston D C and Cheong S-W 1995 *Phys. Rev.* B **52** 15 485
[62] Zibold A M, Tanner D B and Berger H 1998 *Physica* B **244** 27
[63] To calculate the values of n_{tot} and n_{s}, we have used the following structural parameters: $5.4 \times 5.4 \times 13.2$ Å^3, $Z = 4$, $N_{\mathrm{Cu}} = 1$ for La214(O), $5.4 \times 5.4 \times 30.9$ Å^3, $Z = 4$, $N_{\mathrm{Cu}} = 2$ for Bi2212, $3.9 \times 3.9 \times 11.8$ Å^3, $Z = 1$, $N_{\mathrm{Cu}} = 2$ for Y123 and $3.9 \times 3.9 \times 29.4$ Å^3, $Z = 2$, $N_{\mathrm{Cu}} = 2$ for Tl2212. For reference see Hazen R M 1990 *Physical Properties of High Temperature Superconductors II* ed D M Ginsberg (Singapore: World Scientific) p 121
[64] Liu H L 1997 *PhD Thesis* Department of Physics, University of Florida
[65] Yoon Y-D 1995 *PhD Thesis* Department of Physics, University of Florida
[66] Puchkov A V, Fournier P, Timusk T and Kolesnikov N N 1996 *Phys. Rev. Lett.* **77** 1853
[67] Ding H, Norman M R, Yokoya T, Takeuchi T, Randeria M, Campuzano J C, Takahashi T, Mochiku T and Kadowaki K 1997 *Phys. Rev. Lett.* **78** 2628

[68] Uemura Y J *et al* 1989 *Phys. Rev. Lett.* **62** 2317
[69] Uemura Y J *et al* 1991 *Phys. Rev. Lett.* **66** 2665
[70] Uemura Y J *et al* 1993 *Nature* **364** 605
[71] Niedermayer Ch, Bernhard C, Binninger U, Glückler H, Tallon J L, Ansaldo E J and Budnick J I 1993 *Phys. Rev. Lett.* **71** 1764
[72] Tanner D B *et al* 1998 *Physica* B **244** 1